
Article:
Li, Q, Yong, Y, Yang, K et al. (2019) The role of calcium stearate on regulating activation to form stable, uniform and flawless reaction products in alkali-activated slag cement. Cement and Concrete Composites, 103 (29). pp. 242-251. ISSN: 0958-9465

https://doi.org/10.1016/j.cemconcomp.2019.05.009

The role of calcium stearate on regulating activation to form stable, uniform and flawless reaction products in alkali-activated slag cement

Qing Li[a], Yong Yang[a], **Kai Yang[a,b*]**, Zhuo Chao[a], Desha Tang[a], Yi Tian[a], Fang Wu[a], Muhammed Basheer[b], Changhui Yang[a]

a: College of Materials Science and Engineering, Chongqing University, China, 400045
b: School of Civil Engineering, University of Leeds, Leeds, UK, LS29JT

Abstract

In the course of an investigation on using calcium stearate (CaSt) to improve performance of the alkali-activated slag (AAS) cement, the objective of the present work is to discovery its role in the AAS system. Special interest is devoted to understand the influence of CaSt on the reaction process, reaction products and microstructural features of the AAS cement. To achieve this, isothermal calorimetry, impedance characteristics, infrared spectroscopy, X-ray diffraction, thermogravimetry, nitrogen sorption, mercury intrusion porosimetry and scanning electron microscopy were carried out. According to results obtained, the CaSt has three important effects on the AAS cement. Firstly, it inhibited slag reaction with the activator through decreasing activity of alkalis, whereas the amount of C-(A)-S-H gels in the system depended on the usage of CaSt, because the CaSt could have chemical reactions from the alkali-solution and form similar reaction products. Secondly, there is less sodium and more calcium in reaction products of the CaSt added mix, which improve their stability and uniformity. Finally, microstructure characteristics (e.g. pore size distribution, pore connectivity) are optimised and defects are reduced significantly, when the CaSt is added in the AAS mix.

Keywords: alkali-activated slag cement, activation kinetic, calcium stearate, reaction products, microstructure

1.Introduction

Global warming seems to happen faster than we think [1]. Around 5% of anthropogenic CO_2 emissions are caused by the manufacture of Portland cement [2]. Although the proportion of blended cements with lower clinker ratios will keep increasing globally over the last 3 decades [3], it is still difficult to achieve the target, 1.55 Gtpa (gigatonnes per annum) in 2050, recommended by the International Energy Agency (IEA). One reason is that the global demand for cement keeps growing in the near future according to the prediction from the World Cement Association [4,5]. In order to reduce CO_2-emissions, activating industrial by-products that are rich in aluminium and silicon oxide with alkaline to produce clinker-free binder is a promising approach [6-8], especially for steel industry giants such as China [7].

Alkali activation of ground granulated blast-furnace slag (GGBFS) can be defined as a coupled chemical-physical process by dissolution of aluminosilicate vitreous structures in a high pH solution to generate new products forming the rigid skeleton [9]. It can be achieved by different salts under normal temperature. Traditionally, the lime is used, but not widely accepted in the construction industry due to slow strength development [10]. One promising way is to activate with sodium (potassium) carbonate [11], hydroxide or preferably by sodium silicate (water glass) [12], giving suitable alkaline reaction in solution. The principle of the alkali-activation of slag has been known for more than 70 years [13] and the increasing interest in this material has given rise to numerous published reviews and research papers [14-16].

However, even today it remains surprisingly difficult to unambiguously use this binder at an industrial scale. This is in part due to the fact that several classical theories that have been useful in establishing the properties of PC cannot give sufficiently reliable predictions when applied to AAS. Another very real source of difficulty is that the wide range of admixtures developed for PC lost their functions in this system. It means some undesirable performance, such as high shrinkage [17], susceptibility to cracking [18], rapid carbonation [19], high water sorptivity and air permeability [20], cannot be solved by conventional and relatively straightforward techniques. Without in-depth scientific and technical understandings, practical application and social acceptance of AAS are limited despite certain outstanding performance for this low carbon green binder. One dominant feature of the AAS cement is the high risk to form microcracks in reaction products [21]. For this reason, controlling water and gas transport properties, e.g. air permeability and water sorptivity, is not easy with the present knowledge.

As shown by some researchers (e.g. Ge [22], He [23] and Maryoto [24]), calcium stearate (CaSt) is one type of admixtures for the PC system which can adjust the hydration and significantly improve water resistance. Inspired by possibilities of achieving analogous results in AAS, our previously work [25] suggested that CaSt is able to reduce the sorptivity of the AAS cement through optimising microstructure and introducing the hydrophobic film. In that study, macroscopic and microscopic experimental observations have been carried out, and apparent mechanisms are described. However, the main origin of the optimised performance of AAS using CaSt was not given and it is supposed that the improved performance would be the result of changes of the alkali-activation process, characteristics of reaction products and microstructure features. Following the previous work, this study intends to clarify the influence of CaSt on the AAS system. In order to achieve this aim, samples of alkali-activated slag with CaSt were prepared along with AAS and PC samples without CaSt as the reference group. Isothermal calorimetry, impedance characteristics, infrared spectroscopy, X-ray diffraction, thermogravimetry, nitrogen sorption, and scanning electron microscopy were carried out.

2. Experimental programme

2.1 Raw materials

Calcium stearate (CaSt), produced by Chengdu Kelong chemical reagent company, has a density of 1.08g/cm^3 and the particle size ranging from dozens of nanometers to several microns. Its microscopic feature is shown in **Figure 1**.

Ground granulated blast-furnace slag (GGBFS) from Chongqing Iron and Steel Company was used to prepare AAS specimens. After grounding in a ball mill and vibromill, the GGBFS has the specific area of 505 m^2/kg (Blaine fineness) and the density of 2.95 g/cm^3. The PC confirming to the Chinese National Standard GB175-2007 [26] was used to manufacture the comparison specimens as well. Its Blaine fineness and density were 350 m^2/kg and 3.15 g/cm^3. **Table 1** summarises the chemical compositions of the GGBFS and PC.

In this study, the GGBFS was activated by the water glass (liquid sodium silicate) with a modulus 1.5 (n=SiO_2/Na_2O). The alkali solution was prepared by mixing the NaOH solution and water glass (WG) in a pre-calculated ratio (12.2% Na_2O, 30.2% SiO_2 and 46.5% H_2O by mass). In order to avoid potential influences of dissolution heat on experimental results, the alkali solution was placed in a room at a constant temperature of 20 (±1) ^oC for 2 hours prior to mixing.

2.2 Sample preparation

Table 2 gives the mix proportions of AAS and PC samples. In order to reduce local differences, CaSt and GGBFS were premixed in mortar mixer for 60 seconds, after which the alkali solution was added and mixed for another 180 seconds. Specimens were compacted on a vibration table until no air bubbles appeared on the surface and then covered with thick polythene sheets to prevent moisture loss. All specimens were demoulded after one day and placed in the standard curing room (20 (±2) ^oC, relative humidity (RH) > 95%) until the test age.

Two types of specimens were manufactured, Φ50 mm×100 mm cylinders and 40×40×40 mm^3 cubes. The cylindrical specimens were used to extract the pore solution, while the cubic specimens were used for measuring the bulk electrical conductivity and microstructure analysis. The 28-day compressive strength, which had been analysed in our previous work [25], is also given in **Table 2**.

2.3 Test Methods

2.3.1 Isothermal calorimetry

The heat of reaction of AAS and PC samples was assessed using TAM AIR isothermal heat conduction calorimeter. The heat release was measured by comparation between an active (sample) and an inert (sand) cell, both equipped with heat flow sensors. Paste samples with a mass of 15 g were tested. All raw materials were stored at the temperature of 20 °C for 24 hours before mixing. Manual mixing was applied for around 90 seconds with a rod. After this, the sample was placed to the bottom of the measurement cell and then, the samples were directly placed inside the calorimeter. The measurement was carried out every 2 minutes for 120 hours.

2.3.2 Bulk electrical conductivity

The resistivity of paste samples was measured by an LCR bridge (Thonghui LCRbridge-TH2822) using a two-point uniaxial method. Prior to measurements, moisture on the sample surface was removed by a dry towel and samples were placed between two thin parallel metal plates. Two saturated sponges were placed between the metal plate and the specimen in order to achieve an effective contact. Alternating current (AC) with a frequency of 1 kHz was applied to reduce the effect of polarisation. The impedance from the measurements was converted to resistance and the electrical resistivity was calculated using **Equation (1)**:

$$\sigma=(R_{total}-R_{sponge})\frac{A}{l} \qquad (1)$$

where σ is the electrical resistivity ($\Omega\cdot$m); R_{total} is the resistance of a specimen and sponges (Ω); R_{sponge} is the resistance of the sponges (Ω); A is the cross-section area of a specimen (m^2); l is the length of the specimen (m). The resistivity was converted to the conductivity for later analysis.

2.3.3 Pore solution analysis

At the age of 3, 7, 14 and 28 d, the pore solution of paste samples was extracted under a constant pressure of 407.6 MPa (800 kN on 1962.5 mm^2) for 45 minutes. Three specimens were extracted for each mix to ensure the enough pore solution (about 15 ml) can be collected. It is noticed that the strength of specimens at the age of 28 d was so high that little pore solution was collected after the first extraction. Therefore, the second extraction was carried out after crushing the compacted paste. The electrical conductivity of the pore solution was measured immediately using a conductivity probe (Multi 3410 from Germany WTW). The process was taken at a constant room temperature of 20 ^{o}C to minimise the influence of temperature on electrical conductivity. Ion concentration of pore solution at the age of 28d was examined by inductively coupled plasma optical emission spectroscopy (America Thermo from ICP-OES). More details could be obtained in our previously studies [25].

2.3.4 Fourier transform infrared spectroscopy (FTIR)

In order to determine the chemical groups in reaction products, fourier transform infrared analysis was carried out using the KBr pellet method (1 mg sample per 100 mg KBr). The instrument (5DXC from America Nicolet) with 32 scans per sample collected from 4,000 to 400 cm^{-1} at 1 cm^{-1} resolution was set for FTIR measurements. The 28-day paste samples were dried in a blast air oven (Temperature: 40 °C, RH: 20%) for 3 days. Then, the samples were crushed and ground into powders (particle size less than 75 μm) for FTIR tests.

2.3.5 X-ray diffraction (XRD)

Powder samples (curing for 28 days) obtained by the method described above were tested using the XRD. A PANalytical’s XPert Pro X-ray diffractometer with nickel-filtered Cu Kαl radiation 1.5405 Å, 40 kV voltage and 40 mA current with scanning speed of 2°/min was used to identify crystalline phases presented in the samples. The scanned range was between 10° to 80° (2θ).

2.3.6 Thermogravimetric analysis (TGA/DSC)

The TGA/DSC was tested using STA250 (Netzsch, Germany). Samples (curing for 28 days) were crushed, transferred immediately to an alumina crucible and were held under isothermal conditions for 30 min at 20 ^oC to equilibrate in a nitrogen environment. The temperature was raised from the room temperature (20 ± 1 ^oC) to 1000 ^oC with a rate of 5 ^oC/min. The weight change was monitored.

2.3.7 Nitrogen sorption test (NST)

The nitrogen sorption test was carried out using the Micrometics ASAP 2020 Automated Surface Area (Micromeritics Instrument Ltd., America). Paste samples were crushed to particles with the size of about 2.5 mm. The air (water) desorption was performed at 100 ^oC for typically 24 h. The total pore volume was derived from the amount of vapor adsorbed at a relative pressure close to unity. Surface areas were calculated from the isotherm data using the Brunauer-Emmet-Teller (BET) method [27], while mesopore diameter distributions and cumulative pore volumes were determined through the Barret-Joyner-Halenda (BJH) method [27] using desorption data.

2.3.8 Scanning electron microscopy (SEM)

The features of reaction products were assessed by an emission scanning electron microscopy (TESCAN VEGA 3 LMH). The samples were coated with gold to enhance the conductivity. Observations were undertaken at an accelerating voltage of 20 kV with a secondary electron (SE) detector. An energy dispersive spectroscopy (EDS, Oxford instrument) detector at the point scanning mode was used to determine elements in the reaction products.

3. Results and discussion

3.1 Reaction process

3.1.1 Isothermal calorimetry (IC)

The heat flow and cumulated heat release of AAS mixes and PC are given in **Figure 2**. It can be seen from **Figure 2-a** that comparing to the PC, AAS control group has a shorter exothermal activity peak (between 11 and 18 hours). This observation agrees with the higher compressive strength of AAS as shown in **Table 2**, as the short exothermal activity can reflect fast chemical reaction for the binder system. For the AAS mixes with CaSt, similar exothermal activity peaks could be found, but their compressive strength is not as high as the AAS without CaSt. This is due to the fact that CaSt can introduce more closed pores in AAS matrix [25]. **Figure 2-b** shows that the cumulated heat release of AAS groups are lower than that of PC group, similar to the results reported by Gruskovnjak *et al.* [28]. This feature associated with the fact that diffusion is the mechanism which controls the alkaline activation process after the induction period [29] and the induction period of AAS generally comes earlier and lasts shorter than PC (as shown in **Figure 2-a**), leading to a low chemical reaction speed of AAS and cumulated heat release. It is also found that the influence of CaSt on the heat of AAS cement reaction is not significant, except for AAS-45-8%, which gives a slight decrease of cumulative heat beyond 30 hours.

3.1.2 Impedance characteristics and ion concentration

Figure 3 plots the electrical conductivity of the pore solution and the paste samples. From **Figure 3-a**, it can be seen that at the initial period age, the pore solution electrical conductivity of AAS is much higher than that of PC, while the difference between PC and AAS is not significant until 28 days. This feature is not surprising. As shown in previous studies [30], the concentration of ions in the pore solution of PC increased with age because of the releasing ions from hydration reactions, while ions (mainly Na^+, OH^-, SiO_4^{2-}) in the pore solution of AAS were consumed by chemical reactions between alkali-activator and GGBFS [31]. An opposed trend of pore solution electrical conductivity is found for the bulk conductivity of AAS, which is shown in **Figure 3-b**. This is due to the fact that pore structure of AAS is dense and tortuous, resulting in lower bulk electrical conductivity. Detailed discussion is given in our previous work [25] and other researchers' studies, e.g. Ma *et al.* [32], Song *et al.* [33] and Rodriguez *et al.* [33].

Comparation between the results of AAS samples with and without CaSt shows an interesting phenomenon. The pore solution conductivity of AAS decreased after adding CaSt, while the values of AAS-45-4% and AAS-45-8% stay close to each other. The magnitude of pore solution conductivity depends on a number of factors, e.g. ion concentration, temperature and electrolyte [34]. Since the temperature of the solution was maintained at a constant level (20 ^{o}C) in this study, variations induced by CaSt should be caused by changes in other factors. To explore the influence of these factors, **Table 3** gives the ion concentrations of pore solutions obtained from 28-day AAS samples. It is clear that AAS-45-4% and AAS-45-8% have higher Na^+ and Ca^{2+} concentrations than that of AAS-45-0% and this trend is opposed to their low pore solution conductivity, since in general the higher the concentration of ions in solution, the bigger its conductivity should be [35]. In order to understand the features shown in **Figure 3-a**, two additional factors, nature of electrolytes and mobility of ions in the pore solution, should be considered. It is known that the conductivity of the pore solution can be estimated from the concentration of ions and molar conductivity (the conductivity of a solution of unit concentration) [35]. The pore solution of AAS-45-0% only contains strong electrolytes (Na^+, Ca^{2+}, OH^- and SiO_4^{2-}), which means that its molar conductivity generally decreases slightly as the molar concentration increases. In contrast, addition of CaSt might introduce a potential (weak) electrolyte and the characteristic behaviour exhibited is that the molar conductivity of CaSt decreases in a very remarked manner with increasing its concentration. The CaSt is only partially ionised in the pore solution so the number of free ions depends on the concentration in a complicated manner. The conductivity depends on the number of free ions in the solution so for the two CaSt added mixes, it would rely on the degree of dissociation. In other words, the molar conductivity of CaSt decreases rapidly with increasing concentration. Thus, the degree of dissociation should decrease as the CaSt amount increases, and the conductivity of pore solution in the CaSt mixes decreases. Secondly, the transport of ionic species through the pore solution depends on the mobility of ions and the conductivity of pore solution may not be exactly proportional to the number of present ions. As such, the speed of ions' movement has to be considered during the analysis of solution conductivity. Two forces are felt by the ions as they migrate through the pore solution, including an electrical force and a frictional retarding force. The two forces act in opposite directions and once they become balance, the ions in the pore solution would exhibit a net drift speed, which is defined as the ionic mobility [36]. The ionic mobility depends on the size of the moving ions (via the solvated radius), their charge and on the physical properties of the pore solution (via the viscosity [37]). In this study, CaSt was added into the AAS mixes, which is supposed to not only introduce a weak electrolyte but also provide another negative mobile charge ion, $C_{17}H_{35}COO^-$ (the stearate anion). This means that another influencing factor for variation of the pore solution conductivity in the AAS with CaSt is the increase of the solvated radius ($C_{17}H_{35}COO^-$). Hence, the ionic mobility was decreased by CaSt that naturally leaded to a low conductivity.

Further analysis of the pore solution conductivity (**Figure 3-a**) and the concentration of Na^+ and Ca^{2+} (**Table 3**) reveals three additional features. The first one is the difference in the pore solution conductivity, which could partially reflect the alkali-reaction process in these AAS mixes. The second is the increase of Na^+ concentration in the pore solution of CaSt added mixes (shown in **Table 3**). As the initial sodium content is the same for the AAS mixes tested in this study, the high concentration of Na^+ in the pore solution means that there would be less sodium and more calcium in the reaction products, as the accessible porosity of AAS with and without CaSt is close to each other [25]. It is believed that the characteristics of reaction products in the AAS have been modified by CaSt. The third one is the variation in Ca^{2+} that indicates interaction between CaSt and the reaction process in the AAS. The Ca^{2+} in the pore solution may come from two sources-the dissolution of CaSt and decomposition of GGBFS. According to the results from TGA/DSC, it is believed that the Ca^{2+} mainly came from the CaSt (discussed in 3.2.3). That is, the alkali-activation process was modified by CaSt to some degree, whereas these potential changes could not be clearly detected using isothermal calorimetry measurements (shown in **Figure 2**).

Figure 3-b shows that the bulk electrical conductivity of AAS-45-4% and AAS-45-8% was further reduced. This could be the combined result of the decrease of the pore solution conductivity and the low pore connectivity, as reported in the previous work [25].

3.2.1 X-ray diffraction (XRD)

The XRD results of PC and AAS samples after being cured for 28 days at a controlled environment are given in **Figure 4**. It should be pointed out that most chemical reaction products in the AAS samples are C-(A)-S-H gels with amorphous structure, so it is difficult to clearly identify these products due to the influences of background noises. And the XRD results were used to provide certain qualitative indications, especially for the crystal reaction products in the AAS mixes with CaSt. According to **Figure 4-a**, mineralogical characterisation of the reaction products of PC paste shows presence of crystalline portlandite, C-S-H, ettringite and calcite. For AAS pastes, the humps around 30° and 49.5°attributed to C-(A)-S-H can be found. In addition, calcite ($CaCO_3$, 2θ = 29.41°, 39.40° and 43.15°), vaterite ($CaCO_3$, 2θ =27.05°, 32.78° and 50.08°) were detected in the AAS groups as well.

Figure 4-b plots the detailed XRD results of AAS with and without CaSt between 20^o and 40^o. The diffraction curves indicative for calcium carbonate in the AAS with CaSt are not as intense as the control AAS group's, especially for vaterite, which would convert to calcite as the reaction proceeds according to the Ostwald Step Rule [38]. This indicates that the carbonation rate of the AAS samples with CaSt might be slowed. Another important indication in **Figure 4-b** is the difference in the intensity of peaks of X-ray diffractograms around 30°, which offers some indication of the ordering degree of C-(A)-S-H gel [39]. More specifically, the intensity of AAS-4% around 30° is lower than that of AAS-45-0%, while that of AAS-8% is higher. In order to clarify the influence of CaSt on the ordering degree of C-(A)-S-H, the obstruction from the disturbance of calcite cannot be ignored for its characteristic peaks overlapping with that of C-A-S-H gel. The higher intensity of AAS-45-8% around 30^o along with its lower carbonation rate (also detected by FTIR and TGA result), indicates that ordering degree of C-(A)-S-H was improved by CaSt. While the relatively low intensity of AAS-45-4% could be attributed to more calcite formed during sample preparation in AAS-45-0%, which did show the strongest signals of vaterite in **Figure 4-a**. The result also highlights that ordering degree of C-A-S-H in AAS-45-8% is higher than that of AAS-45-4%. In addition, the higher Na^+ concentration in the pore solution of CaSt added mixes and less sodium in reaction products also give indirect evidences. As shown in experimental results from Ye *et al.* [21], Lothenbach and Nonat [40], sodium can be taken up in the interlayer space preferentially at low calcium concentrations and high pH values, and the less sodium could improve the regularity of the stacking of the C-(A)-S-H layers.

3.2.2 Fourier transform infrared spectroscopy (FTIR)

FTIR was carried out to estimate the relative quantity of reaction and chemical reaction products by differentiating the typical wave numbers and corresponding transmittance. **Figure 5-a** shows the infrared spectra of AAS and PC samples at the age of 28 days. The main difference bestween PC and AAS is that the band at 3654 cm^{-1} in the PC sample cannot be found in the AAS groups. This wave number relates to the O-H stretching of portlandite [41] and the result suggests the absence of portlandite in the AAS mixes. In addition, three bands at 1471 cm^{-1}, 1419 cm^{-1}, and 876 cm^{-1} can be found in all samples, which correspond to the anti-symmetric stretching and out-of-plane bending modes of CO_3^{2-} ions [41].

Further comparison of the results between the AAS samples with and without CaSt highlights two additional absorptions, around 2918 cm^{-1} and 2850 cm^{-1}. The two absorptions can be assigned to the asymmetric and symmetric stretching vibrations of the CH_2 group [42]. In order to illustrate the impact of CaSt, details at the range from 1600 to 400cm^{-1} are given in **Figure 5-b**, from which three distinguishing features for AAS with CaSt could be identified. Firstly, two additional adsorption peaks, 1578 and 1541 cm^{-1}, can be found in AAS-45-4% and AAS-45-8% that correspond to COO^- in CaSt [42] and the transmittance of AAS-45-8% is higher than that of AAS-45-4% due to more CaSt added. Secondly, the low intensity of the bands at 1471,1419 and 876 cm^{-1} for the AAS with CaSt (AAS-45-4% and AAS-45-8%) can be observed, which indicates that relatively limited carbonation products can be found in these two groups. Lastly, the intensity of the C-(A)-S-H bands (974 and 453 cm^{-1}) depends on the amount of CaSt added in the AAS mix. More specifically, the quantity of C-(A)-S-H gels in AAS-45-4% is close to the AAS control group, while the AAS-45-8% would have less gels than that in the other two mixes. Overall, the results shown in **Figure 5-b** suggests that the CaSt would affect the characteristics and quantity of reaction products in the AAS and its influence depends on the usage.

3.2.3 Differential thermogravimetry

Figure 6 shows the TGA/DSC results of sole CaSt, PC and AAS samples. The data in **Figure 6-a** gives basic characteristics of CaSt. The endothermic peak at 107 ^{o}C is detected corresponding to evaporative water, while the endothermic peak at 123 ^{o}C can be attributed to the melt of CaSt for no weight change in TGA curve in this temperature range. The decomposition of RCOO$^-$ can be detected at 432 ^{o}C, 482 ^{o}C accompanying by large weight loss in TGA, while some calcium carbonate in CaSt could be found (the endothermic peak: around 680 ^{o}C [45]).

In order to minimise the influence of evaporable moisture and poorly absorbed moisture in samples, the temperature range of TGA/DSC from 100 to 1000 ^{o}C is selected. The TGA curves can be divided into three regions and the weight loss of the four regions are summarised in **Table 4**. The main findings in each region are given:

1) The first region (I), temperature from 100 to 530 ^{o}C: The main difference between the PC and AAS mixes is that PC has two major absorption peaks, 152 and 462 ^{o}C, which cannot be found in the AAS groups. The weight changes observed at these two temperatures correspond to the dehydroxylation of ettringite (152 ^{o}C) and portlandite (462 ^{o}C) [43] and it is reasonable that the AAS groups do not have these reaction products. According to the research result of Haha *et al.* [44], weight loss of AAS samples at this region could be proportional to the quantity of chemical reaction products. Additional peaks around 432 ^{o}C, 487 ^{o}C for AAS-45-4% and 411 ^{o}C, 491 ^{o}C for AAS-45-8% can be found in DSC curves. This associates with the decomposition of CaSt (RCOO$^-$) [45]. The specific values agree well with the amount of CaSt added in the mix, 3.1% for AAS-45-4% and 6.4% for AAS-45-8% estimated according results in **Figure 6-a**. **Table 4** summarises the weight loss of PC and AAS mixes after removing the influence of CaSt decomposition. It could be found that the weight loss of AAS-45-4% is close to that of the AAS control group in this region, suggesting a similar amount of main chemical reaction products. It agrees with the FTIR results given in **Figure 5**. The weight loss of AAS-45-8% is lower than that of the other two AAS groups, which is believed due to the inhibition influence of CaSt on the reaction process.
2) The second region (II), the temperature from 530 to 800 ^{o}C: All mixes have a detectable weight loss and the corresponding temperature range in **Figure 6-b** also exhibits slightly different endothermic peaks (692 ^{o}C, 696 ^{o}C, 702 ^{o}C, 707 ^{o}C respectively for PC, AAS-45-0%, AAS-45-4%, AAS-45-8%) which reflect the decarbonation of calcium carbonate [45]. It is also noticed that the weight change of the CaSt added AAS mixes can come from the degradation of CaSt [46], and specific values is 0.45% for AAS-5-4% and 0.95% for AAS-5-8% (calculated according results in **Figure 6-a**). After removing its influence, the weight loss results of all samples are given in **Table 4**. It can be seen that PC and AAS-45-0% show lager weight change, while the weight change in AAS-45-4% and AAS-45-8% is relatively small. This indicates that AAS with CaSt should have a relatively low degree of carbonation.
3) The third region (III), the temperature higher than 800 ^{o}C: Valuable information could be obtained from **Figure 6-b** at the temperature range of 826-846 °C, in which the area of exothermic peaks for AAS-45-4% and AAS-45-8% is higher than that for AAS-45-0% that reflects the content of glassy state substance in unreacted slag [47]. According to these results, it can be deduced that there is more unreacted slag in AAS-45-4% and AAS-45-8%. This could be attributed to the inhibition influence of CaSt on the chemical reaction between alkali-solution and GGBFS. This observation seems to give a controversy conclusion in comparison with the results presented in **Figure 5**, in which a similar amount of reaction products is found for AAS-45-0% and AAS-45-4%. Combining with the results in the pore solution analysis (**Figure 2** and **Table 3**), it is believed that the additional chemical reaction products in

AAS-45-4% would come from further reactions caused by CaSt with the alkali solution. This explains why less GGBFS reacted, but more chemical reaction products are formed.

3.3 Characteristics of microstructures and defects

3.3.1 Nitrogen sorption test (NST)

Figure 7 plots the curves of sorption isotherms against relative pressure (P/P_o). Cumulative pore volumes and pore distributions determined through BJH method are given in **Figure 8-a** and **-b** respectively. From the adsorption curves, the AAS control group adsorbs less nitrogen gas than that of the PC sample, which could be attributed to its low porosity and disconnected pores [48]. Furthermore, the AAS samples with CaSt tend to adsorb even less nitrogen, which may be due to the fact that the pores become less disconnected as reported in the previous study [25]. Meanwhile, cumulative pore volume of AAS with CaSt tends to decrease as the CaSt amount increase. This trend is also reflected by the pore size distribution data, shown in **Table 5**. The pores diameter less than 4.2 nm is 2.41%, 15.82%, 19.45% and 38.51% for PC, AAS-45-0%, AAS-45-4%, and AAS-45-8% respectively. It suggests that the CaSt is helpful to dense pore structure of the AAS at micropore level (the pore size is classified according to recommendations given by the IUPAC [49]).

The specific surface was estimated from the N_2 adsorption test, the results of which is reported in **Table 5**. As expected, the specific area of AAS is higher in comparison with the PC group. This observation agrees with the results reported by Provis *et al.* [48] and Song *et al.* [33]. The specific surface area of AAS-45-4% reaches 35.7 m^2/g, while the trend of optimising microstructure is not observed for AAS-45-8%, as the specific area decreases compared with that of AAS-45-4%. It is believed that the results associate with less reaction products in AAS-45-8%. Due the limited applicability of N_2 sorption test when evaluate the pore structure, only fine capillary pore is assessed and more information about the characterization of coarse pores analysed by MIP could be seen in our previous work [25].

3.3.2 Scanning electron microscopy (SEM) and optical observation

One main drawback of the AAS cement is the high risk of cracking, which significantly affect its performance, especially for durability. In order to assess the influence of CaSt on the AAS system, the microstructure of AAS with/without CaSt was examined using SEM and the results are shown in **Figure 9**. Clearly, lots of cracks could be found in the AAS control group, which agrees well with the results of Marjanović *et al.* [50] and Yang *et al.* [51]. According to Collins and Sanjayan [18], Morandeau *et al.* [52], the great cracking tendency could be attributed to rapid drying process, which leads to rapid moisture loss within gel pores of AAS and resulting in a significant volumetric change. The microstructure of AAS-45-4% and AAS-45-8% is given in **Figure 9-a** and **-b**. When the magnification was increased to 20,000X (shown in **Figure 9 d-f**), there are lots of nanoscale pores (darker portion) within the matrix (brighter portion) in the control group. As shown in the figure, few cracks can be found in AAS samples with CaSt and the microstructure of CaSt added samples becomes denser. Many CaSt particles, as marked in red circles, can be found within matrix as well. The results indicate that the CaSt did reduce the micro-defects of AAS. After adding CaSt, the gel pore is refined and become disconnected [25], thus the rate of moisture loss is reduced. Meanwhile, the deposits of CaSt are found on the surface of pores and there are some large pores in the CaSt added samples, which may be due to its air maintaining function. The third mechanism for modification of cracking is that less alkalis are incorporated into reaction products. According to the research results of Ye *et al.* [21], the micro-cracks in the AAS may be attributed to the instability of reaction products with high alkali cations, which makes the gels easier to collapse and redistribute during the drying process. The chemical reaction products of CaSt added mix has less incorporated alkalis that reduces the alkalis-terminated sites inside C-A-S-H gels, which served as additional available locations (as a vacancy defects) for microstructure rearrangement [21]. Thus, few micro-cracks are found in AAS-45-4% and AAS-45-8%.

In order to provide quantitative information, 100 SEM images (275μm×275μm) were randomly selected at different locations from each mix and cracking features were analysed by counting the number of cracks, measuring length and width of cracks and calculating total cracking area. The results are summarised in **Table 6**. Clearly, the cracking area drop nearly 40% from 163815 μm^2 to 102743 μm^2 when CaSt was added, and the best performance is obtained for AAS-45-4%. Another important feature is that the max crack width in the AAS is decreased by 50% and the average crack width reduced from 2.6 μm to 1.5 μm. It is noticed that there are more cracks in AAS-45-4% and AAS-45-8%, but most micro-cracks in AAS-45-4% and AAS-45-8% are short and narrow and hence, the low cracking area is found, which is clearly reflected in **Figure 9-b** and **-c**.

4. Conclusions

Addition of CaSt is a promising approach to improve the performance of the AAS cement and clarification of the role of CaSt in the AAS is essential to understand root causes for the enhanced performance. The aim of the present paper is to contribute new results to this subject, while on the basis of results obtained, the following conclusions could be made:

1) The CaSt plays an essential role to control the reaction process through interactions within the AAS system. It is reflected by the fact that more unreacted GGBFS can be found in the mixes with CaSt, although the quantity of reaction products in AAS-45-4% is very close to the reference group (AAS-45-0%). It should be pointed out that the isothermal calorimetry is not sensitive to detect this feature.
2) Analysis of Na^+ and Ca^{2+} concentrations in the pore solution suggests that these two elements in reaction products of AAS with CaSt vary considerably. Using CaSt made much less sodium incorporated into the reaction products and there might be more calcium in the reaction products. This feature can assist in improving uniformity and stability of reaction products, as shown in the XRD and TGA/DSC results.
3) The results of N_2 adsorption indicate that the microstructure of AAS became dense, when CaSt was added. It is clear that the CaSt is able to reduce microcracking according to analysis of the SEM results. As shown, 4% of CaSt seems to be optimal for the AAS in this study.
4) Numerous CaSt can be found on the surface of pores from the SEM images. Although it is not easy to differentiate if the CaSt on the pore surface is due to chemical or physical binding because of limited analytical technique available, the hydrophobic film is very helpful to reduce the water sorptivity, as shown in the previous study.
5) One feature obtained from the TGA, XRD and FTIR results is that there were few carbonation products in the AAS with CaSt. Poor resistance against carbonation is one main drawback for the AAS cement and clearly, more research is needed to confirm essential results.

Acknowledgements

The authors acknowledge the following institutions for providing facilities and the financial support: National Natural Science Foundation of China (NO. 51878102 and 51778089), Open funds from Shenzhen University, Venture and innovation support program for Chongqing oversea returns. In addition, supports provided from University of Leeds during analysis of data and preparation of this paper are also highly appreciated.

References

[1] Y. Y. Xu, V. Ramanathan and D.G. Victor, Global warming will happen faster than we think, Nature. 564 (2018) 30-32.

[2] H. Mikulcic´, N. Markovska, M. Vujanovic´, R. V. Filkoski and M. Ban, N. Duić, Potential for CO_2 emission reduction in the cement industry, in: Digital Proceedings of the 7th Conference on Sustainable Development of Energy, Water and Environment Systems–SDEWES Conference. Ohrid, Makedonija, 2013, 35(2), 703-708.

[3] R. M. Andrew, Global CO_2 emissions from cement production, Earth System Science Data. 10 (2018) 195-217. https://doi.org/10.5194/essd-10-195-2018.

[4] J. Revill, Global cement demand forecast to grow 1.5 percent in 2019, Business News, Reuters, Dec 5 (2018), https://in.reuters.com/article/us-cement-forecast/global-cement-demand-forecast-to-grow-15-percent-in-2019-idINKBN1O425

Z.

[5] F. Pacheco-Torgal, J. Castro-Gomes and S. Jalali, Alkali-activated binders: A review-Part 1. Historical background, terminology, reaction mechanisms and hydration products, Construction and Building Materials. 22 (2008) 1305-1314.

[6] A. Palomo, P. Krivenko, I. Garcia-Lodeiro, E. Kavalerova, O. Maltseva and A. Fernández-Jiménez, A review on alkaline activation: new analytical perspectives, Materiales De Construccion. 64 (2014), http://dx.doi.org/10.3989/mc.2014.00314.

[7] China Concrete and Cement-based Products Association (CCPA), 2017 annual development report of slag industry. (2018)

[8] T. Bakharev, J. G. Sanjayan and Y-B Cheng, Alkali-activated slag of Australian slag cements, Cement and Concrete Research. 29 (1999) 113-120.

[9] J. L. Provis, Alkali-activated materials, Cement and Concrete Research. 114 (2017) 40-48.

[10] K-H Yang, A-R Cho, J-K Song and S-H Nam, Hydration products and strength development of calcium hydroxide-based alkali-activated slag mortars, Construction and Building Materials. 29 (2012) 410-419.

[11] A. F. Abdalqader, F. Jin and A. Al-Tabbaa, Development of greener alkali-activated cement: utilisation of sodium carbonate for activating slag and fly ash mixtures, Journal of Cleaner Production. 113 (2016) 66-75.

[12] B. S. Gebregziabiher, R. Thomas and S. Peethamparan, Very early-age reaction kinetics and microstructural development in alkali-activated slag, Cement and Concrete Composites. 55 (2015) 91-102.

[13] P. Duxson, A. Fernández-Jiménez, J. L. Provis, G. C. Lukey, A. Palomo and J. S. J. van Deventer, Geopolymer technology: the current state of the art, Journal of Materials Science. 42 (2006) 2917-2933.

[14] R. J. Myers, S. A. Bernal and J. L. Provis, Phase diagrams for alkali-activated slag binders, Cement and Concrete Research. 95 (2017) 30-38.

[15] B. M. Mithun, M. C. Narasimhan, P. Nitendra and A.U. Ravishankar, Flexural fatigue performance of alkali-activated slag concrete mixes incorporating copper slag as fine aggregate, Journal of Civil Engineering. 10 (2015) 7-18.

[16] A. M. Rashad, D. M. Sadek and H. A. Hassan, An investigation on blast-furnace stag as fine aggregate in alkali-activated slag mortars subjected to elevated temperatures, Journal of Cleaner Production. 112 (2016) 1086-1096.

[17] H. L. Ye, C. Cartwright, F. Rajabipour and R. Aleksandra, Understanding the drying shrinkage performance of alkali-activated slag mortars, Cement and Concrete Composites. 76 (2017) 13-24.

[18] F. Collins and J. G. Sanjayan, Cracking tendency of alkali-activated slag concrete subjected to restrained shrinkage, Cement and Concrete Research. 30 (2000) 791-798.

[19] N. Li, N. Farzadnia and C. Shi, Microstructural changes in alkali-activated slag mortars induced by accelerated carbonation, Cement and Concrete Research. 100 (2017) 214-226.

[20] K. Yang, C. H. Yang, B. Magee, S. Nanukuttan and J. X. Ye, Establishment of a preconditioning regime for air permeability and sorptivity of alkali-activated slag concrete, Cement and Concrete Composites. 73 (2016) 19-28.

[21] H. L. Ye and A. Radlińska, Shrinkage mechanisms of alkali-activated slag, Cement and Concrete Research. 88 (2016) 126-135.

[22] Z. Ge, Concrete admixture [Second edition], Chemical industry publishing house. Beijing (2015) 187-188.

[23] T. He, Concrete admixture, Shanxi science and technology publishing house. Xi'an (2013) 165-166.

[24] A. Maryoto, Resistance of concrete with calcium stearate due to chloride attack tested by accelerated corrosion, Procedia Engineering. 171 (2017) 511-516.

[25] Q. Li, K. Yang and C. H. Yang, An alternative admixture to reduce sorptivity of alkali-activated slag cement by optimising pore structure and introducing hydrophobic film, Cement and Concrete Composites. 95 (2019) 183-192.

[26] GB-175, Common Portland cement, Standardization Administration of the People's Republic of China. Beijing (2007) 6 pages.

[27] Z. Zhang, Y. Zhua, H. Zhu, Y. Zhang, J. L. Provis and H. Wang, Effect of drying procedures on pore structure and phase evolution of alkali-activated cements, Cement and Concrete Composites. 96 (2019) 194-203.

[28] A. Gruskovnjak, B. Lothenbach, L. Holzer, et al., Hydration of alkali-activated slag: comparison with ordinary Portland cement, Advances in Cement Research. 18 (2006) 119-128.

[29] A. Fernández-Jiménez, F. Puertas, Alkali-activated slag cements: kinetic studies, Cement and Concrete Research. 27 (1997) 359-368.

[30] L. Z. Xiao, Z. J. Li, Early-age hydration of fresh concrete monitored by non-contact electrical resistivity measurement, Cement and Concrete Research. 38 (2008) 312-319.

[31] J. C. Kim, S. Y. Hong, Liquid concentration changes during slag cement hydration by alkali activation, Cement and Concrete Research. 31 (2001) 283-285.

[32] Q. M. Ma, S. V. Nanukuttan, P. A. M. Basheer, Y. Bai and C.H. Yang Chloride transport and the resulting corrosion of steel

bars in alkali-activated slag concretes, Materials and Structures. 49 (2016) 3663-3677.

[33] S. Song, D. Sohn, H. M. Jennings and T. O. Mason, Hydration of alkali-activated ground granulated blast-furnace slag, Journal of Materials Science. 35 (2000) 249-257.

[34] K. A. Snyder, X. Feng, B. D. Keen and T. O. Mason, Estimating the electrical conductivity of cement paste pore solutions from OH^-, K^+ and Na^+ concentrations, Cement and Concrete Research. 33 (2003) 793-798.

[35] F. Rajabipour and J. Weiss, Electrical conductivity of drying cement paste, Materials and Structures. 40 (2007) 1143-1160.

[36] P. T. PH Nye, Solute movement in the soil-root system, Blackwell Scientific Publications, Oxford, UK, 1977.

[37] S. N. Malakhov, S. I. Belousov, A. V. Bakirov, and S. N. Chvalun, Electrospinning of Non-Woven materials from the melt of polyamide-6 with added magnesium, calcium, and zinc stearates, Fibre Chemistry. 47 (2015) 14-19.

[38] S. A. Bernal, J. L. Provis, D. G. Brice, A. Kilcullen, P. Duxson and J. S. J. van Deventer , Accelerated carbonation testing of alkali-activated binders significantly underestimates service life: The role of pore solution chemistry, Cement and Concrete Research. 42 (2012) 1317-1326.

[39] R. J. Myers, S. A. Bernal, J. D. Gehman, J. S. J. van Deventer and J. L. Provis, The Role of Al in cross-linking of alkali-activated slag cements, Journal of the American Ceramic Society. 98 (2015) 996-1004.

[40] B. Lothenbach and A. Nonat, Calcium silicate hydrates: Solid and liquid phase composition, Cement and Concrete Research. 78 (2015) 57-70.

[41] B. Lu, C. Shi, J. Zhang and J. Wang, Effects of carbonated hardened cement paste powder on hydration and microstructure of Portland cement, Construction and Building Materials. 186 (2018) 699-708.

[42] Y. Q. Lu and J. D. Miller, Carboxyl stretching vibrations of spontaneously adsorbed and LB-transferred calcium carboxylates as determined by FTIR internal reflection spectroscopy, Journal of Colloid and Interface Science. 256 (2002) 41-52.

[43] Z. Pavlík, A. Trník, T. Kulovaná, L. Scheinherrová, V. Rahhal, E. Irassar and R. Cerný, DSC and TG analysis of a blended binder based on waste ceramic powder and Portland cement, International Journal of Thermophysics. 37 (2016)

[44] M. B. Haha, B. Lothenbach, G. Le Saout and F. Winnefeld, Influence of slag chemistry on the hydration of alkali-activated blast-furnace slag-Part II: Effect of Al_2O_3, Cement and Concrete Research. 42 (2012) 74-83.

[45] Y. Liang, K. Y. Yu, Q. Z. Zheng, J. Xie and T. Wang, Thermal treatment to improve the hydrophobicity of ground $CaCO_3$ particles modified with sodium stearate, Applied Surface Science. 436 (2018) 832-838.

[46] Y. Lin, H. B. Chen, C. M. Chan and J. S. Wu, Nucleating effect of calcium stearate coated $CaCO_3$ nanoparticles on polypropylene, Journal of Colloid and Interface Science. 354 (2011) 570-576.

[47] V. Kocaba, E. Gallucci and K. L. Scrivener, Methods for determination of degree of reaction of slag in blended cement pastes, Cement and Concrete Research. 42 (2012) 511-525.

[48] J. L. Provis, R. J. Myers, C. E. White, V. Rose and J. S.J. van Deventer, X-ray microtomography shows pore structure and tortuosity in alkali-activated binders, Cement and Concrete Research. 42 (2012) 855-864.

[49] F. Collins and J. G. Sanjayan, Effect of pore size distribution on drying shrinkage of alkali-activated slag concrete, Cement and Concrete Research. 30 (2000) 1401-1406.

[50] N. Marjanović, M. Komljenović, Z.Baščarević, V. Nikolić and R. Petrovićb, Physical-mechanical and microstructural properties of alkali-activated fly ash-blast furnace slag blends, Ceramics International. 41 (2015) 1421-1435.

[51] L. Y. Yang, Z. J. Jia, Y. M. Zhang and J.G. Dai, Effects of nano-TiO_2 on strength, shrinkage and microstructure of alkali activated slag pastes, Cement and Concrete Composites. 57 (2015) 1-7.

[52] A. E. Morandeau, J. P. Fitts, H. D. Lee, S. M. Shubeita, L. C. Feldman, T. Gustafsson and C. E. White, Nanoscale heterogeneities in a fractured alkali-activated slag binder: A helium ion microscopy analysis, Cement and Concrete Research. 79 (2016) 45-48.

Figures and Tables

Table1 Chemical composition of GGBFS and PC (by mass %)

Binder	SiO_2	Al_2O_3	Fe_2O_3	MgO	CaO	Na_2O	K_2O	SO_3	LOI	Other composition
GGBFS	32.12	13.65	1.36	9.15	36.47	0.35	0.47	0.26	0.57	5.6
PC	22.54	5.47	2.64	2.74	62.10	0.61	0.18	0.57	3.14	<0.05

Table 2 Paste mixture proportions (per liter of paste)

Parameters	Mix notation			
	PC	AAS-45-0%	AAS-45-4%	AAS-45-8%
W/B	0.45	0.45	0.45	0.45
NaOH pellets (g)	--	20.4	20.4	20.4
Sodium silicate (g)	--	184.6	184.6	184.6
Water (g)	405	346.1	346.1	346.1
Cement (g)	900	--	--	--
Slag (g)	--	900	900	900
CaSt (g)	--	0	36	72
28d-Compressive strength (MPa)	42.4	53.1	46.2	39.3

Note: 1) The modulus of water glass (SiO_2/Na_2O) is 1.5; 2) The density of water glass is 1.05 g/cm^3; 3) A constant alkaline concentration (Na_2O equivalent: 5% by mass of GGBFS) is used in this study.

Table 3 Summary of Na^+ and Ca^{2+} concentrations in the pore solution of AAS samples at the age of 28d

Mix notation	Ion concentration (mg/L)	
	Na^+	Ca^{2+}
AAS-45-0%	25102	2.786
AAS-45-4%	25992	4.342
AAS-45-8%	25858	3.286

Table 4 Weight loss of PC and AAS samples of 28d curing at a given temperature region

Mix notation	Mass loss (%)		
	Region I (100~530 ^{o}C)	Region II (530~800 ^{o}C)	Region III (800~1000 ^{o}C)
PC	11.7	4.6	0.3
AAS-45-0%	10.6	3.6	0.5
AAS-45-4%	10.6	2.1	0.2
AAS-45-8%	9.9	2.3	0.1

Note: The influence of decomposition of CaSt on the results was removed.

Table 5 Summary of pore structure characteristics obtained from NST (curing for 28d)

Mix notation	Pore size distribution (%)		Specific surface area (m^2/g)
	<4.2nm	＞4.2nm	
PC	2.41%	97.59%	24.8
AAS-45-0%	15.82%	84.18%	31.7
AAS-45-4%	19.45%	80.55%	35.7
AAS-45-8%	38.51%	61.49%	27.2

Note: 1) Specific surface area is estimated from the N_2 adsorption measurements.

Table 6 Summary of micro-cracking features obtained from SEM images (all samples curing for 28d)

Mix notation	Total crack number	Total crack area (μm^2)	Maximum crack width (μm)	Average crack width (μm)
AAS-45-0%	458	163815	9	2.6
AAS-45-4%	503	102743	4.5	1.5
AAS-45-8%	516	126915	4.5	1.8

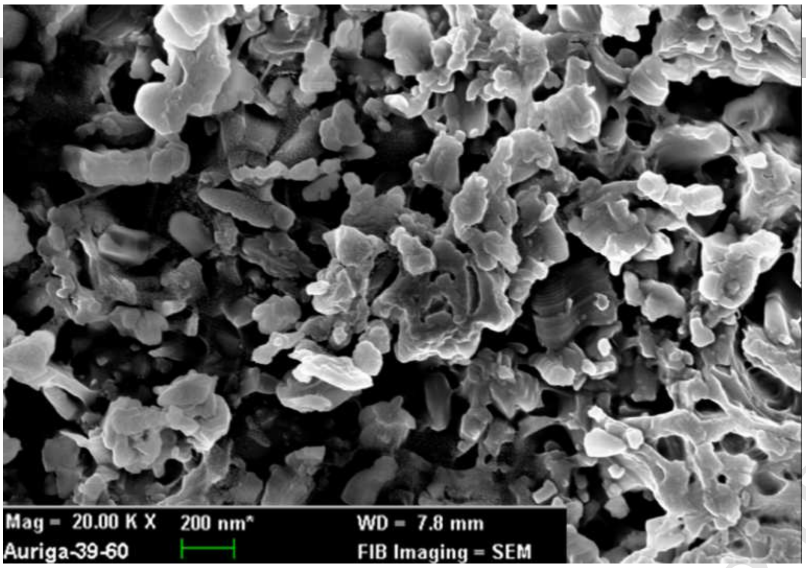

Figure 1 Microscopic feature of calcium stearate

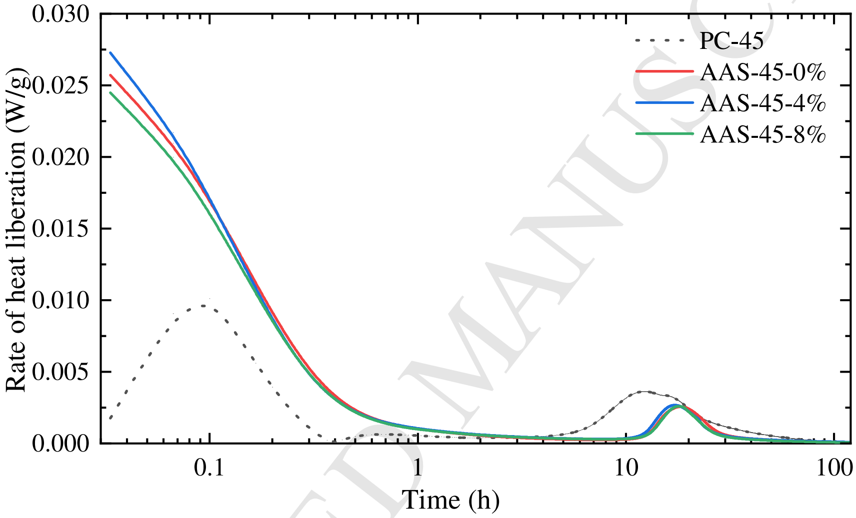

(a) Heat flow evolution

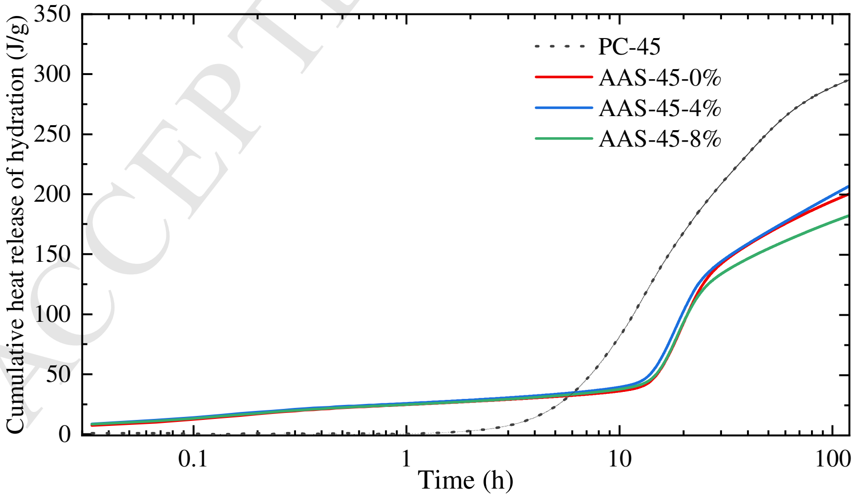

(b) Cumulated heat release

Figure 2 Isothermal calorimetry data for PC and AAS samples

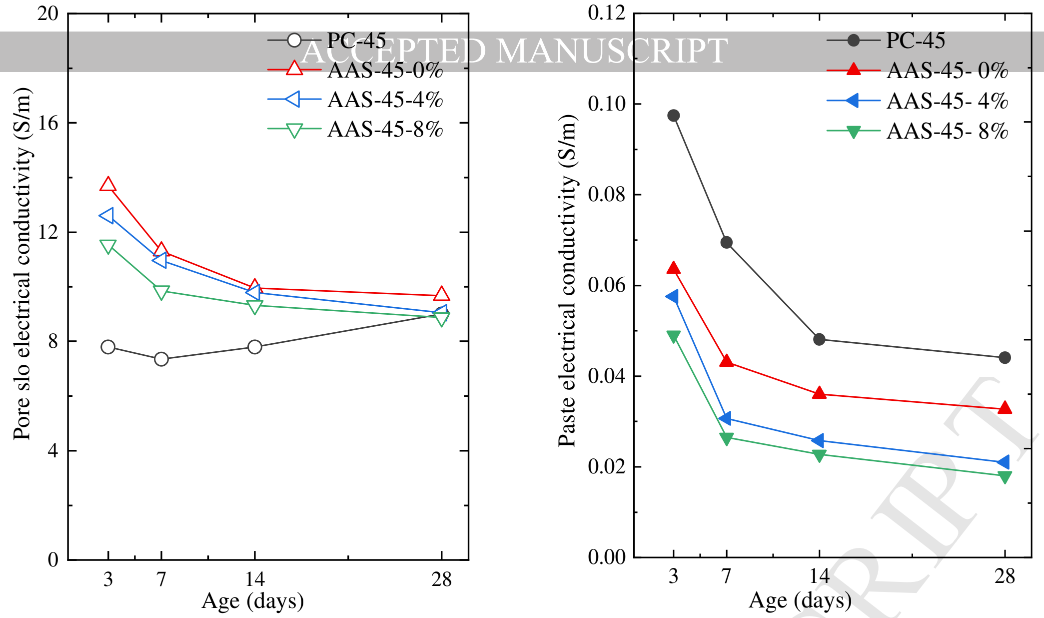

(a) Pore solution electrical conductivity

(b) Paste bulk electrical conductivity

Figure 3 Impedance characteristic data of PC and AAS samples

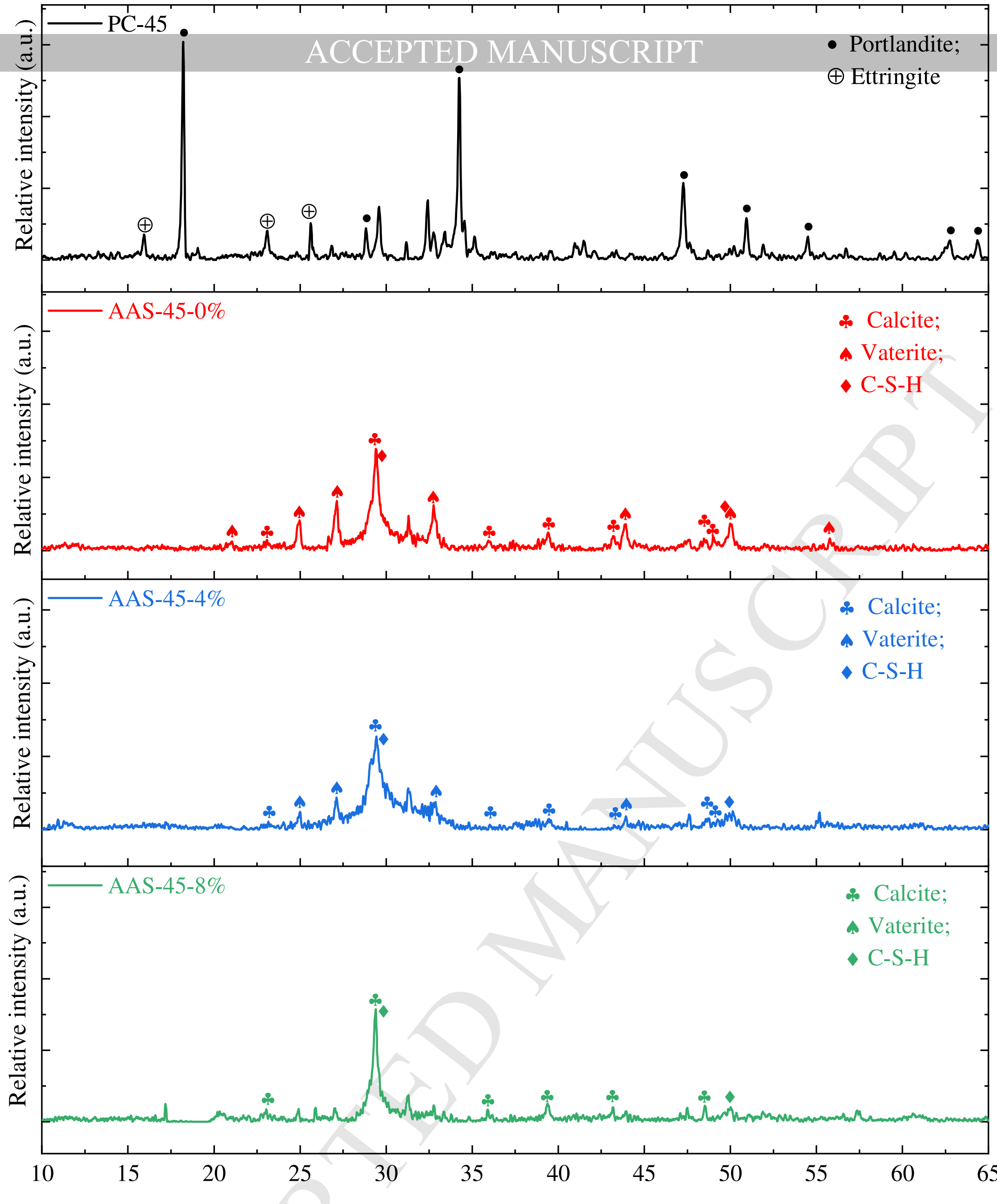

(a) XRD patterns of PC and AAS pastes with and without CaSt

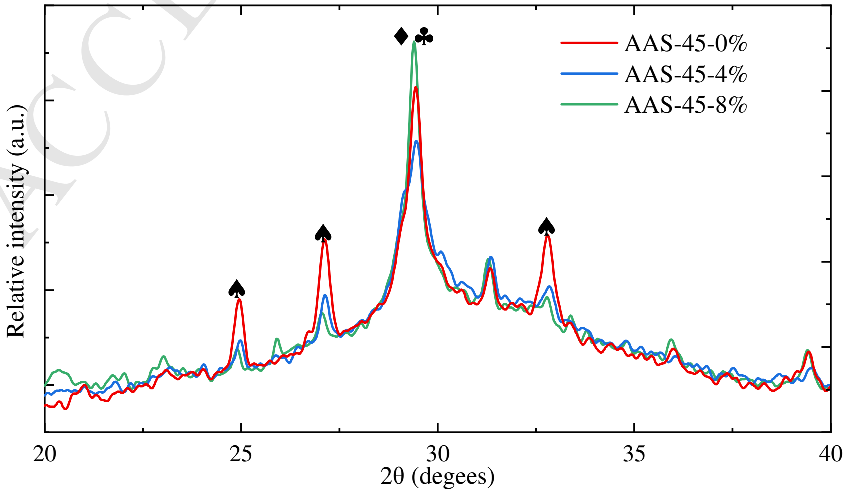

(b) Comparison of XRD patterns for AAS pastes with and without CaSt (2θ: in range of 20-40°)

Figure 4 XRD results of PC and AAS samples at the age of 28d

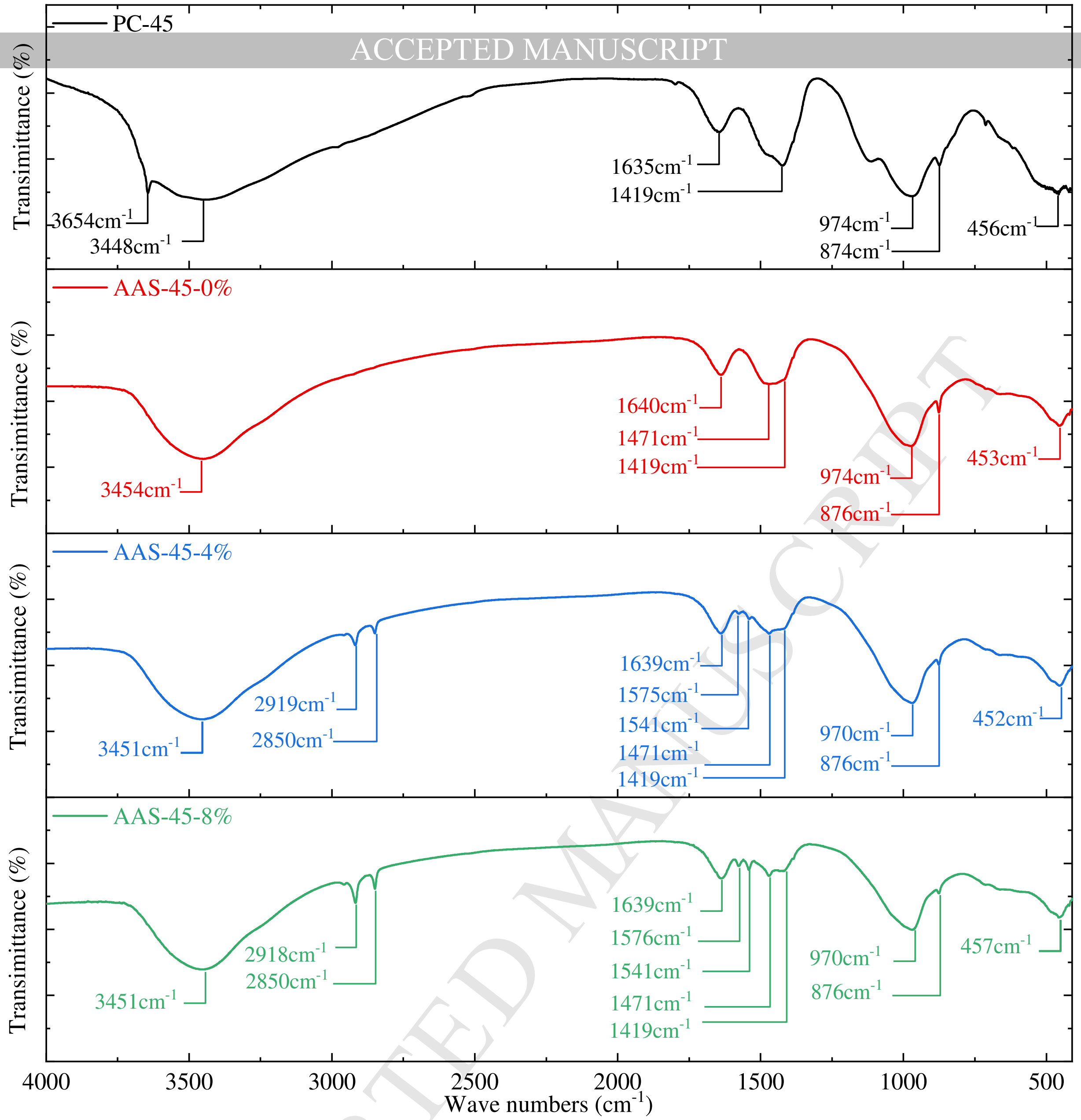

(a) FTIR patterns of PC and AAS pastes with and without CaSt

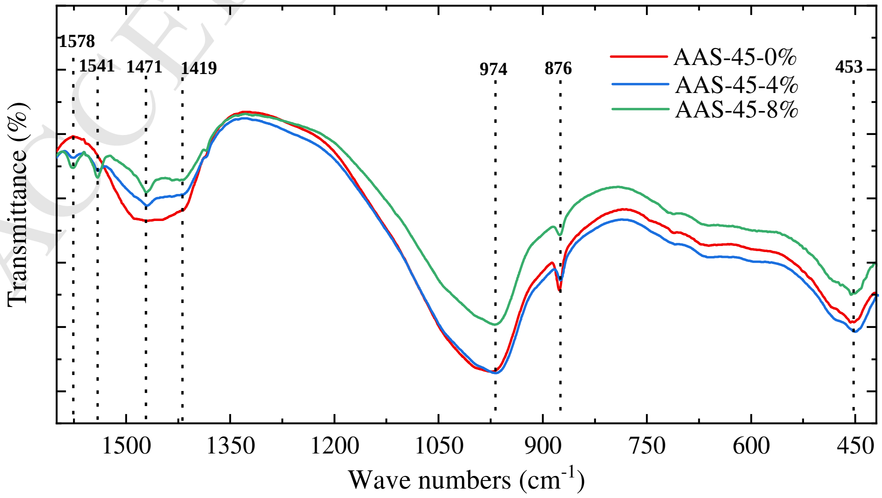

(b) Comparison of FTIR patterns for AAS pastes with and without CaSt (Wave numbers: in range of 420-1600 cm^{-1})

Figure 5 FTIR results of PC and AAS samples at the age of 28d

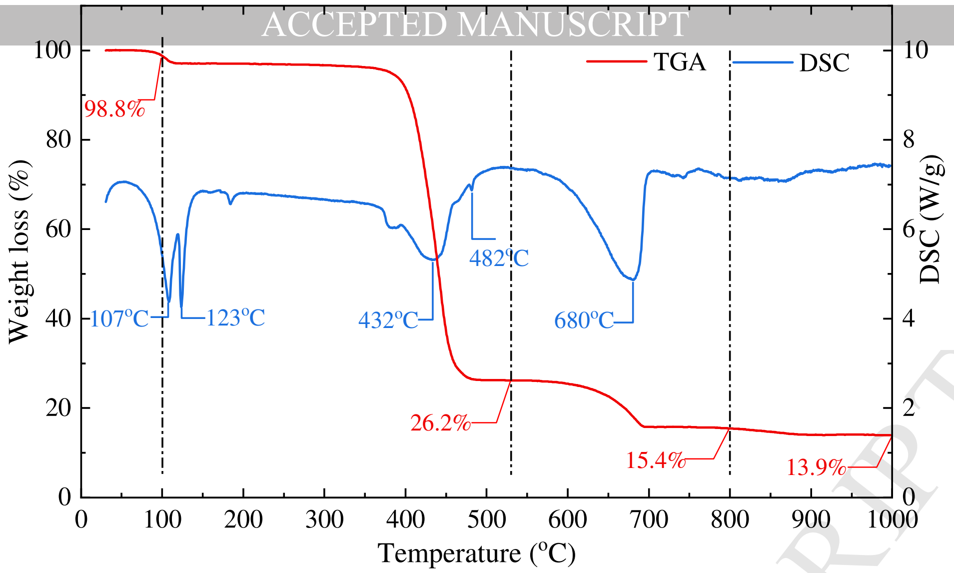

(a) Thermogravimetric (TGA/DSC) results of CaSt

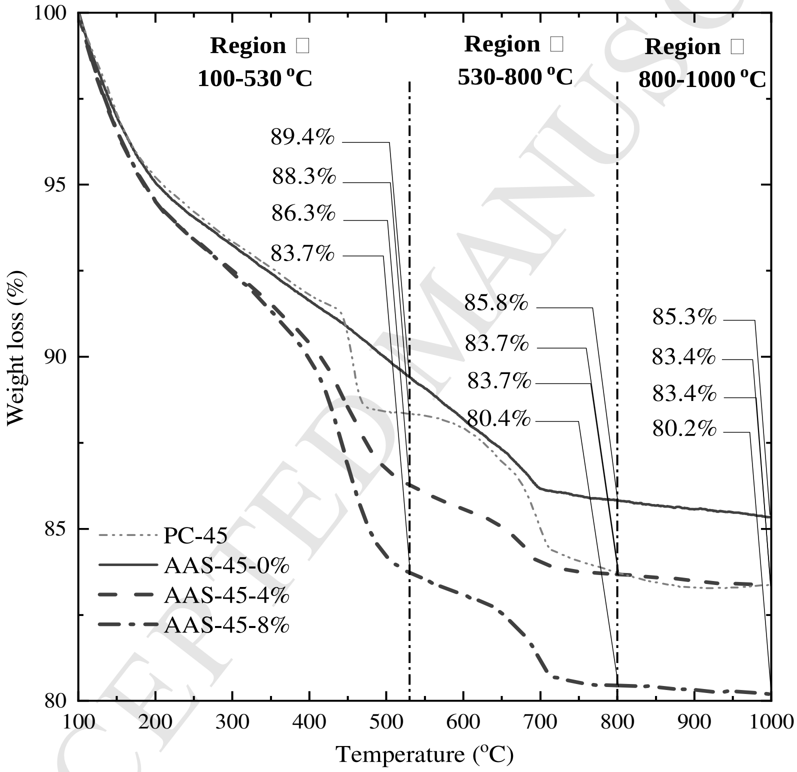

(b) Plot of weight loss against temperature

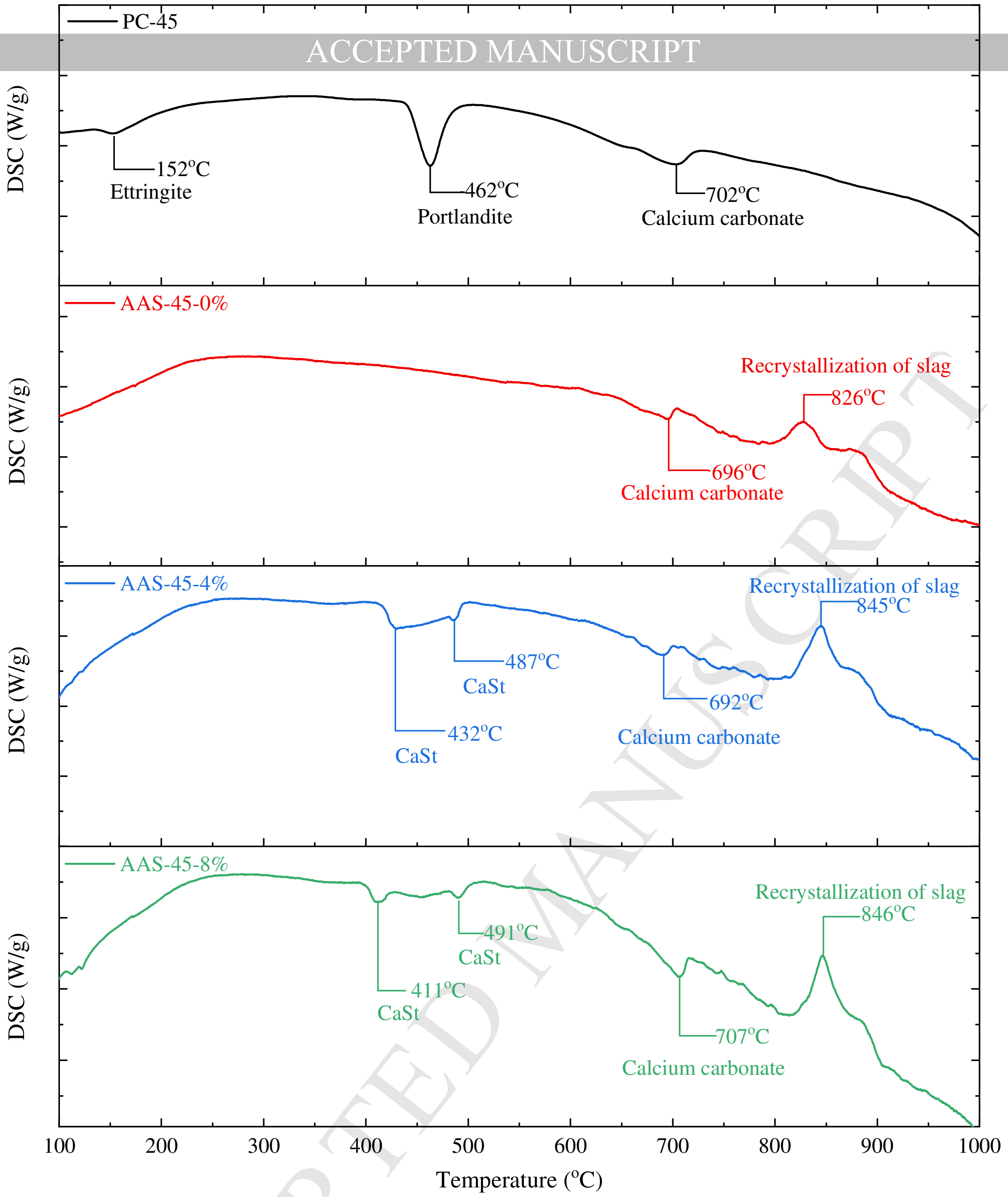

(c) Plot of calorimeter peak against temperature

Figure 6 TGA/DSC results of the CaSt, PC and AAS samples at the age of 28d

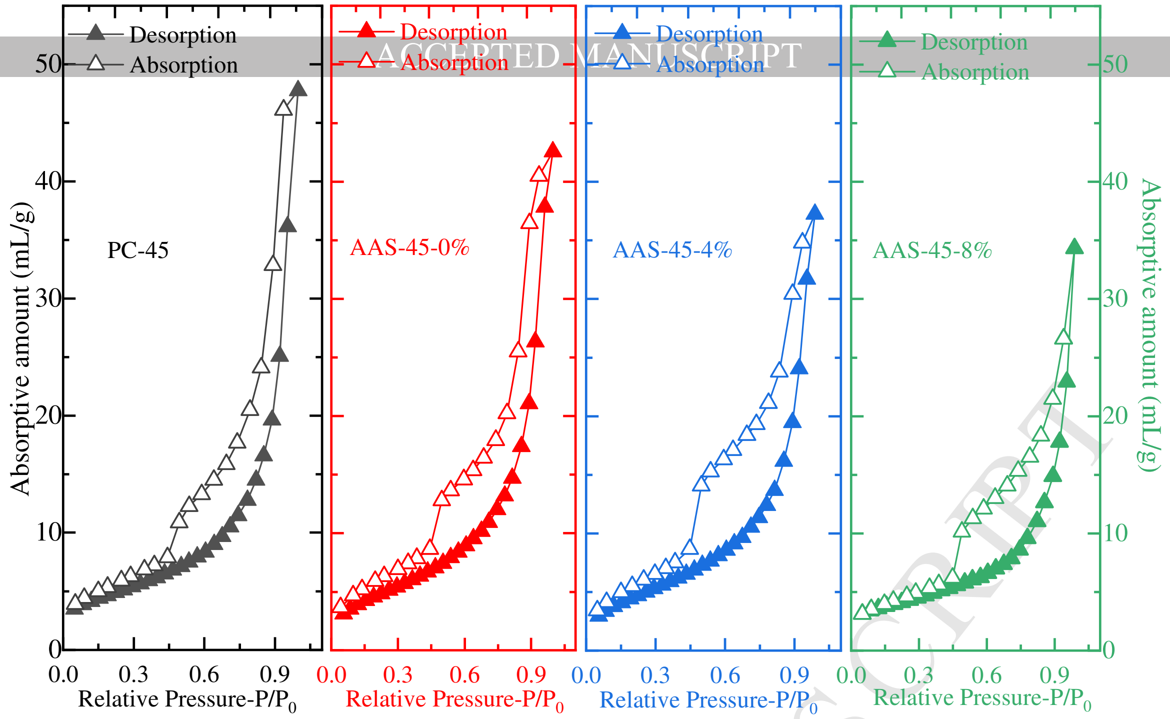

Figure 7 Sorption and desorption curves of PC and AAS samples

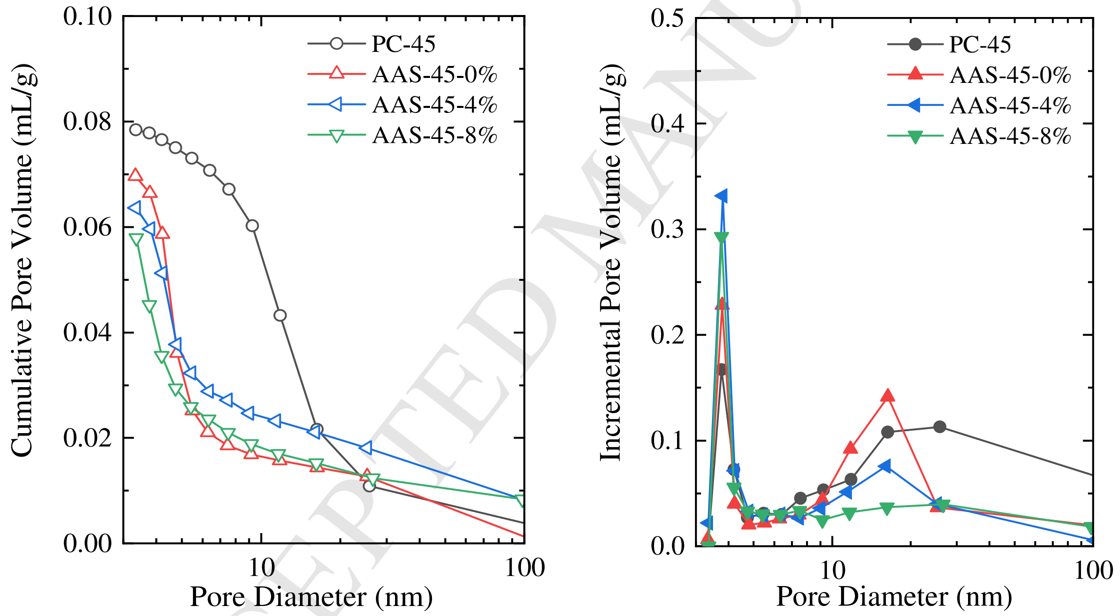

(a) Cumulative pore volume **(b)** Incremental pore volume

Figure 8 Pore structure characteristics of PC and AAS samples at the age of 28d

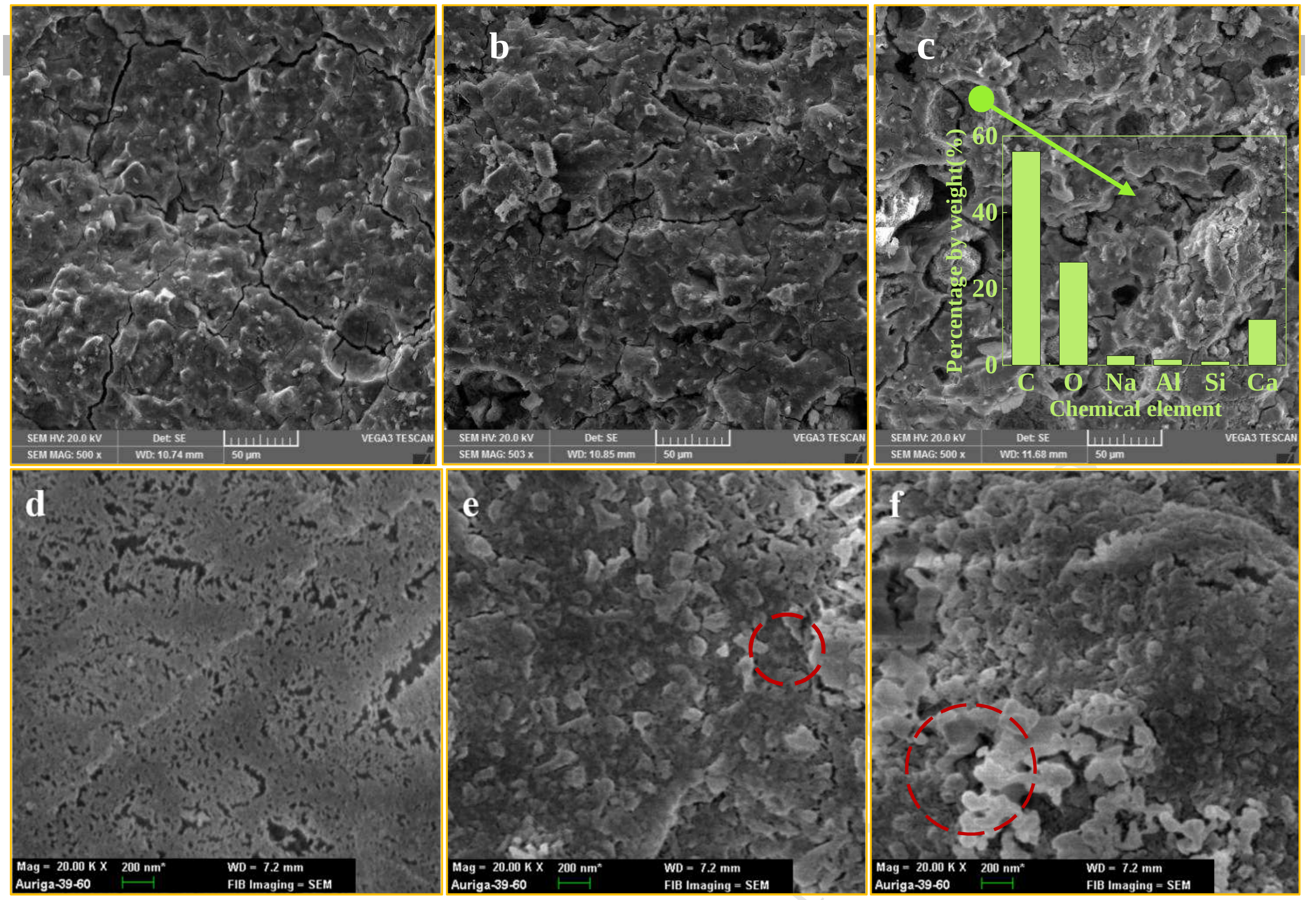

Figure 9 SEM images of AAS samples at different magnification
(a) AAS-45-0%-500X; **(b)** AAS-45-4%-500X with EDS; **(c)** AAS-45-8%-500X;
(d) AAS-45-0%-20000X; **(e)** AAS-45-4%-20000X; **(f)** AAS-45-8%-20000X